Carbon-Based Supercapacitors Produced by Activation of Graphene

Yanwu Zhu,[1] Shanthi Murali,[1] Meryl D. Stoller,[1] K. J. Ganesh,[1] Weiwei Cai,[1] Paulo J. Ferreira,[1] Adam Pirkle,[2] Robert M. Wallace,[2] Katie A. Cychosz,[3] Matthias Thommes,[3] Dong Su,[4] Eric A. Stach,[4] Rodney S. Ruoff[1]*

Supercapacitors, also called ultracapacitors or electrochemical capacitors, store electrical charge on high-surface-area conducting materials. Their widespread use is limited by their low energy storage density and relatively high effective series resistance. Using chemical activation of exfoliated graphite oxide, we synthesized a porous carbon with a Brunauer-Emmett-Teller surface area of up to 3100 square meters per gram, a high electrical conductivity, and a low oxygen and hydrogen content. This sp^2-bonded carbon has a continuous three-dimensional network of highly curved, atom-thick walls that form primarily 0.6- to 5-nanometer-width pores. Two-electrode supercapacitor cells constructed with this carbon yielded high values of gravimetric capacitance and energy density with organic and ionic liquid electrolytes. The processes used to make this carbon are readily scalable to industrial levels.

Supercapacitors store energy by forming a double layer of electrolyte ions on the surface of conductive electrodes. Supercapacitors are not limited by the electrochemical charge transfer kinetics of batteries and thus can operate at very high charge and discharge rates and can have lifetimes of over a million cycles (*1*). However, the energy stored in supercapacitors is currently an order of magnitude lower than that of batteries, which limits their adoption to those applications that require high cycle life and power density. The energy density of existing state-of-the-art supercapacitor devices, which are mainly based on porous activated carbon (AC), is about 4 to 5 watt-hour (Wh)/kg, whereas that of lead acid batteries is in the range of 26 to 34 Wh/kg (*2*). A typical AC material, with a Brunauer-Emmett-Teller (BET) specific surface area (SSA) in the range of 1000 to 2000 m^2/g and a pore size distribution in the range of 2 to 5 nm, has a gravimetric capacitance of 100 to 120 F/g in organic electrolytes (*3*). Research has thus been focused on increasing energy density without sacrificing cycle life or high power density (*4*). An increased capacitance in the organic electrolyte tetraethylammonium tetrafluoroborate (TEA BF_4) in acetonitrile (AN) by using carbide-derived carbons (CDCs) has been reported (*5*). Metal oxides such as RuO_2 or MnO_2 (*6*), MoO_3 (*7*), and electronically conducting polymers (*8*), or their composites, have been used to increase specific capacitance via pseudo-capacitive redox reactions. Although capacitances of up to 1300 F/g (such as with MnO_2) have been reported in aqueous electrolytes (*9*), the low electrical conductance, poor compatibility with organic electrolytes, and short cycle life have limited the practical application of these pseudo-capacitive materials. Carbon nanotubes (CNTs), especially single-walled CNTs (SWNTs), have an ideal limit SSA of 1300 m^2/g (*10*), can have high electrical conductance along the tubes, and demonstrate good performance in organic electrolyte (*11*). However, the high cost for mass production of high-quality SWNTs is a challenge for the commercialization of SWNT-based supercapacitors.

Graphene has a theoretical SSA of 2630 m^2/g and a very high intrinsic electrical conductivity in plane as well as high mechanical strength and chemical stability (*12*). Graphene-based material derived from graphite oxide (GO) is now being manufactured in ton quantities at low cost (*13*). We have previously demonstrated supercapacitors that were based on reduced graphene oxide with capacitance values of approximately 130 and 100 F/g in aqueous KOH and organic electrolytes, respectively (*14*). With a low equivalent series resistance (ESR), the supercapacitor performance did not show much degradation with an increase in the scan rate. Various graphene-based materials derived from GO have reported

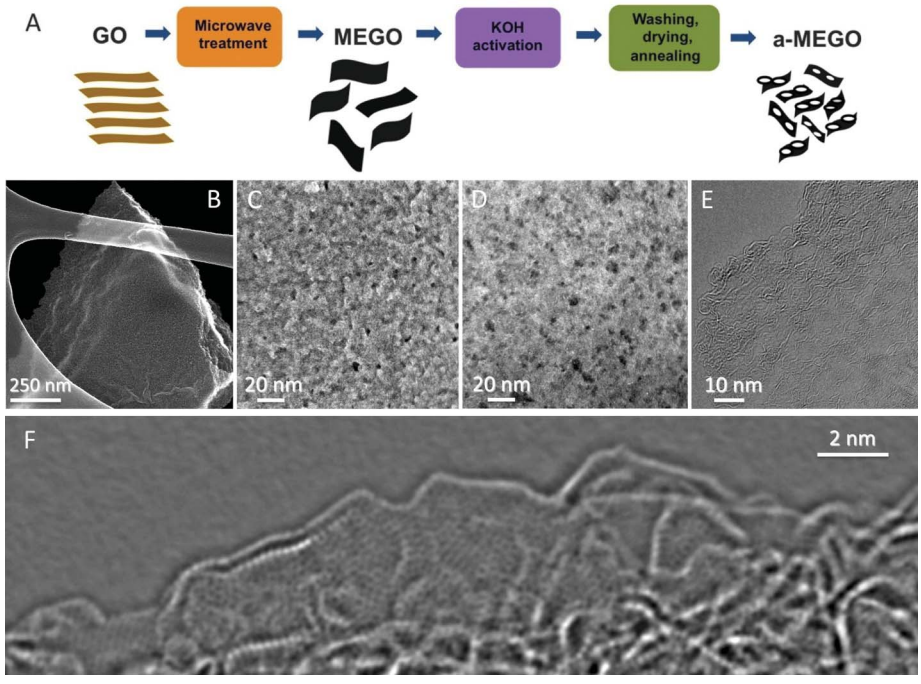

Fig. 1. (**A**) Schematic showing the microwave exfoliation/reduction of GO and the following chemical activation of MEGO with KOH that creates pores while retaining high electrical conductivity. (**B**) Low-magnification SEM image of a 3D a-MEGO piece. (**C**) High-resolution SEM image of a different sample region that demonstrates the porous morphology. (**D**) ADF-STEM image of the same area as (C), acquired simultaneously. As seen, a-MEGO contains micro- and mesopores with a distribution of sizes between ~1 and ~10 nm. (**E**) High-resolution phase contrast electron micrograph of the thin edge of an a-MEGO chunk, taken at 80 kV. There is a variation in focus across the image because of the sloped nature of the sample and changes in sample thickness. The image shows the presence of a dense network of nanometer-scale pores surrounded by highly curved, predominantly single-layer carbon. (**F**) Exit wave reconstructed HR-TEM image from the edge of a-MEGO. The in-plane carbon atoms are clearly resolved, and a variety of *n*-membered carbon rings can be seen. Substantial curvature of the single-carbon sheets is visible, with the in-plane crystallinity being preserved.

[1]Department of Mechanical Engineering and Materials Science and Engineering Program, University of Texas at Austin, One University Station C2200, Austin, TX 78712, USA. [2]Department of Materials Science and Engineering, University of Texas at Dallas, 800 West Campbell Road, Richardson, TX 75080, USA. [3]Quantachrome Instruments, 1900 Corporate Drive, Boynton Beach, FL 33426, USA. [4]Center for Functional Nanomaterials, Brookhaven National Laboratory, Upton, NY 11973, USA.

*To whom correspondence should be addressed. E-mail: r.ruoff@mail.utexas.edu

high-end capacitance values of ~200 F/g in aqueous electrolytes (*15*, *16*), ~120 F/g in organic electrolytes (*16*, *17*), and ~75 F/g in an ionic liquid (*18*). Recently, supercapacitors using oriented graphene grown on nickel by means of chemical vapor deposition were reported (*19*) that demonstrated efficient filtering of 120 Hz current with a resistance capacitance (RC) time constant of less than 0.2 ms, but at the cost of effective energy storage because of the very low density of the electrode material.

To date, the reported SSA values of carbon materials derived from GO have been well below 2630 m^2/g. Here, we report a simple activation with KOH of microwave exfoliated GO (MEGO) and thermally exfoliated GO (TEGO) to achieve SSA values up to 3100 m^2/g. As described in (*20*), we prepared MEGO powders by irradiating GO in a microwave oven. The as-made MEGO powder was then placed in KOH solution, followed by filtration and drying, to form a series of MEGO/KOH mixtures for chemical activation. Each MEGO/KOH mixture was put in a tube furnace under flowing argon at a pressure of about 400 torr and heated at 800°C for 1 hour. A schematic of this activation process is shown in Fig. 1A. Chemical activation has been extensively used to obtain porous ACs (*21*). KOH activation has been used on CNTs (*22*), carbon nanofibers (*23*), and polyacrylonitrile-carbon nanotube composites (*24*), and improved porosity and enhanced supercapacitor performance were reported. It is suggested that the activation of carbon with KOH (*25*) proceeds as $6KOH + C \leftrightarrow 2K + 3H_2 + 2K_2CO_3$, followed by decomposition of K_2CO_3 and/or reaction of $K/K_2CO_3/CO_2$ with carbon.

The activation with KOH generated nanoscale pores in the product carbon. The SSA of the activated MEGO (a-MEGO) could be readily controlled by the ratio of KOH versus MEGO (fig. S1). The scanning electron microscopy (SEM) image in Fig. 1B shows the morphology of a typical a-MEGO piece. Figure 1 shows high-resolution SEM (Fig. 1C), annular dark field scanning transmission electron microscopy (ADF-STEM) (Fig. 1D), and high-resolution TEM (HR-TEM) (Fig. 1, E and F) images of the microstructure. These images [and additional images (fig. S2 and movie S1)] clearly indicate that the activation process etches the MEGO and has generated a three-dimensional (3D) distribution of what are referred to as meso- and micropores in the porous materials literature. The activation with KOH yields a continuous 3D network of pores of extremely small size, ranging from ~1 nm to ~10 nm. Thus, it appears that the chemical activation is not merely digesting the MEGO but also dramatically restructuring it. (The 3D nature of these very small pores makes a statistically accurate quantitative analysis with EM of the distribution of pore sizes difficult because not all pores are visible in a given image.) The spherical aberration–corrected HR-TEM image presented as Fig. 1E (taken at 80 kV so as to prevent electron beam damage) further corroborates a dense pore structure with a continuous three-dimensional network of highly curved, predominantly atom-thick walls. An exit-wave reconstructed image (Fig. 1F) taken with the Transmission Electron Aberration-Corrected Microscope (TEAM) instrument (spherical and chromatic aberration correction, at 80 kV) clearly resolves the individual carbon atoms in the structure. This image shows that a-MEGO is composed of *n*-membered rings in plane, with *n* varying between 5 and 8. Additionally, it is clear that even as the walls bend through high degrees of curvature the in-plane crystallinity is preserved.

Electron paramagnetic resonance (EPR) data (fig. S3) indicate an unpaired spin count at the parts-per-million level. This—in hand with the very low H and O content in the a-MEGO indicated by elemental analysis—shows that a-MEGO has a small fraction of edge atoms. (If a large fraction of the C were edge atoms, they would either be functionalized or would be present as "dangling bonds" that would register an EPR signal.)

Characterization of a sample of a-MEGO by means of synchrotron powder x-ray diffraction (XRD) and x-ray photoelectron spectroscopy (XPS) is shown in Fig. 2, A and B. Comparison with MEGO indicates that the (002) peak of a-MEGO has a markedly reduced intensity and is dramatically broadened. These results are consistent with the observations from HR-TEM, which indicate that a-MEGO is composed of predominantly single-carbon sheets: Thus, a strong decrease in the (002) peak would be expected. A large increase in the low-angle scatter from a-MEGO versus MEGO is also noted, which is consistent with the presence of a high density of pores. In the XPS C1*s* spectrum of MEGO shown in Fig. 2B, the tail between 286 and 290 eV is due to C-O groups and energy loss "shake-up" features (*26*). These oxygen-containing groups were strongly suppressed after activation, with two new peaks appearing between 292 and 296 eV in the a-MEGO sample that were assigned as K2*p* peaks. The K2*p* peaks (<2 atomic % as determined from XPS) in a-MEGO are due to potassium residue, primarily as K_2CO_3 with a small amount of KOH. Quantification of the amount of sp^2-bonding can be determined by measuring the ratio between π* bonding and π* + δ* bonding by using electron energy loss spectroscopy (EELS) (*27*). A comparison of the carbon K near-edge structure for a-MEGO and graphite of equivalent thickness is presented in Fig. 2C. With the assumption that the sp^2 bonding in the graphite reference spectra is 100%, the a-MEGO was found to have 98% (±2%) sp^2 bonding. Complementary measurements were also made by XPS, reaching similar conclusions (further details of the fitting procedures can be found in fig. S4). Micro Raman spectroscopy (fig. S5A) and Fourier transform infrared spectroscopy (fig. S5B) are provided for completeness but did not supply additional insights about a-MEGO beyond the other methods of analysis discussed here.

State-of-the-art surface and pore-size characterization of the a-MEGO was performed by

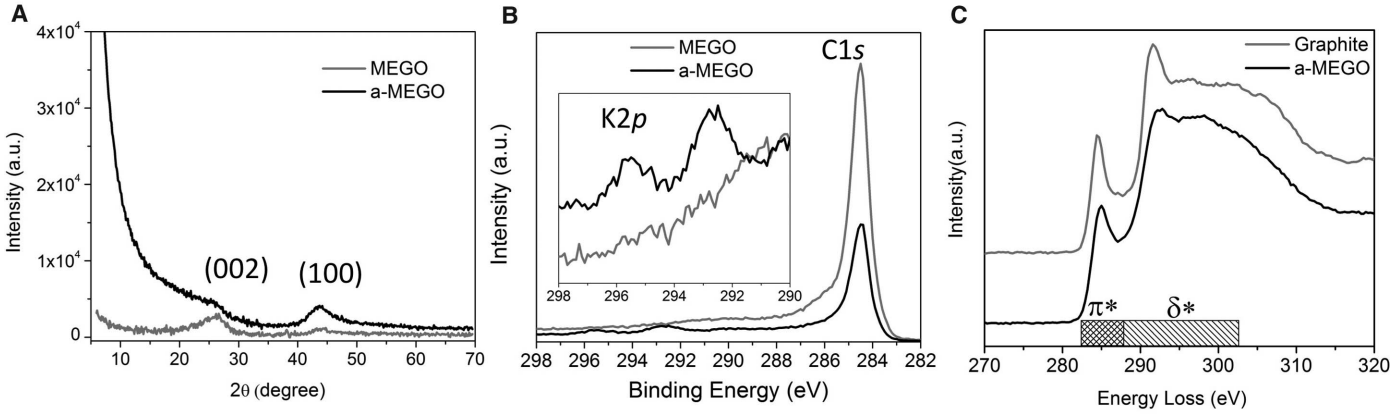

Fig. 2. Characterization of the a-MEGO material (SSA ~ 2520 m^2/g) with MEGO or graphite as a control. (**A**) Synchrotron powder XRD pattern (plotted as Cu Kα). Full width at half maximum of the (100) peak is ~2 degrees for both samples, indicating average in-plane crystal size of ~5 nm with the Scherrer equation; the reduction of the (002) in a-MEGO indicates that there are essentially no interlayer correlations of the carbon sheets. (**B**) XPS C1*s* spectra, with K2*p* region in the inset. (**C**) EELS spectra from a-MEGO and graphite. Quantification of the near-edge structure indicates that the a-MEGO has 98% (±2%) sp^2 bonding.

coupling high-resolution nitrogen (77.4 K) and argon (87.3 K) adsorption/desorption experiments with advanced methods based on density functional theory (DFT) (*28*). In addition, CO_2 adsorption at 273.2 K has been performed to assess the ultramicropores (pores of width <1 nm). These isotherms, as shown in Fig. 3A, reveal the details of the low-pressure region in which micropore filling occurs, as well as the linear plot of the argon and nitrogen isotherms that reveal pore condensation and type H2 hysteresis [according to the International Union of Pure and Applied Chemistry (IUPAC) classification] (*29*) for the a-MEGO sample, which is indicative of an interconnected pore system exhibiting constrictions (*29*, *30*). For comparison, nitrogen adsorption on a MEGO control sample is also shown in fig. S6, and it is evident that the pore volume of MEGO is much smaller than that of a-MEGO; the small overall pore volume should be caused by the platelet-like structure in MEGO—likely just the gap between platelets (*20*). In contrast, the pores in a-MEGO have a well-defined micro-mesopore size distribution as shown in Fig. 3B, with a huge increase in pore volume (up to 2.14 cm^3/g) relative to MEGO. The a-MEGO had a high nitrogen BET SSA of ~3100 m^2/g (calculated in the linear relative pressure range from 0.1 to 0.3). Within this context, in a strict sense the BET method is not applicable to microporous solids, and hence the obtained BET surface area should be considered as an apparent or equivalent area only. Figure 3B displays the results of the cumulative pore volume and pore size analysis from CO_2 and nitrogen adsorption by applying a hybrid nonlocal DFT (NLDFT) kernel, assuming a slit pore geometry for the micropores and a cylindrical-pore geometry for the mesopores, which appears (although oversimplified) to be a reasonable assumption also with regard to the SEM/STEM/TEM results. The obtained pore-size/volume distribution indicates that this carbon sample is distinctive because of the existence of well-defined micro- and mesopores. The presence of ultramicropores is seen from the CO_2 data, and the analysis of the nitrogen adsorption data reveals the presence of micropores in the ~1-nm size range as well as narrow mesopores centered around 4 nm in size. The latter is in good agreement with the bimodal distribution of pore sizes observed with high-resolution EM images. A quenched solid DFT (QSDFT), which quantitatively accounts for the surface roughness (*31*), also has been used to obtain the pore-size distribution of a-MEGO from the nitrogen and argon adsorption data, as shown in fig. S7. The pore size distribution curves obtained from argon and nitrogen agree very well.

Using best-practice methods for determining an electrode material's performance for supercapacitors (*32*), we constructed and measured the performance of two-electrode symmetrical supercapacitor cells on the basis of a-MEGO (SSA ~ 2400 m^2/g) and 1-butyl-3-methyl-imidazolium tetrafluoroborate (BMIM BF_4)/AN electrolyte, as shown in Fig. 4. The cyclic voltammetry (CV) testing (Fig. 4A) shows rectangular curves from 0 to 3.5 V over a wide range of voltage scan rates. The galvanostatic charge/discharge curves at three current densities are shown in Fig. 4B. The specific capacitance was calculated from the discharge curves with values of 165, 166, and 166 F/g obtained at current densities of 1.4, 2.8, and 5.7 A/g, respectively. The corresponding volumetric capacitance is ~60 F/cm^3. The voltage drop at the initiation of the discharge is 0.034 V (for the current density of 1.4 A/g), suggesting a very low ESR in the test cell. A frequency response analysis (FRA) of the frequency range from 500 kHz to 5 mHz yields the Nyquist plot shown in Fig. 4C. The plot features a vertical curve, indicating a nearly ideal capacitive behavior of the cell. From the magnified data in the high-frequency range (Fig. 4C, inset), a transition between the RC semicircle and the migration of electrolyte was observed at a frequency of about 382 Hz, corresponding to a resistance of 2.45 ohms. The diffusion of electrolyte ions stopped at about 3 Hz, and thereafter the whole capacitance was reached (*33*). The voltage drop at the beginning of discharge curves was used to estimate the internal resistance. An ESR of 3.2 ohms was obtained from a-MEGO in the BMIM BF_4/AN electrolyte. Based on a series RC model, the capacitance from the FRA data as a function of frequency is shown in Fig. 4D. The capacitance decreases sharply at about 4 Hz and remains 0.035 F at 10 Hz. Supercapacitor performance of the a-MEGO (SSA ~ 3100 m^2/g) in the TEA BF_4/AN electrolyte was also measured and yielded a specific capacitance of above 150 F/g as obtained from the discharge curve with a constant current of 0.8 A/g, with an ESR of 4.6 ohms (fig. S8). One other carbon (KOH-activated CDCs) using the same AN-based electrolyte with comparable specific capacitance values has been reported (*34*). a-MEGO has the highest gravimetric capacitance in organic electrolyte reported to date for any carbons derived from graphene-based materials.

Values for energy and power density were estimated on the basis of the supercapacitor measurements in the BMIM BF_4/AN electrolyte. Using the specific capacitance value of 166 F/g (from the discharge curve with a constant current of 5.7 A/g) and working voltage of 3.5 V, the energy density is ~70 Wh/kg for the a-MEGO in the cell. Based on a weight ratio of 30% for the active electrode material in a packaged supercapacitor device—typical

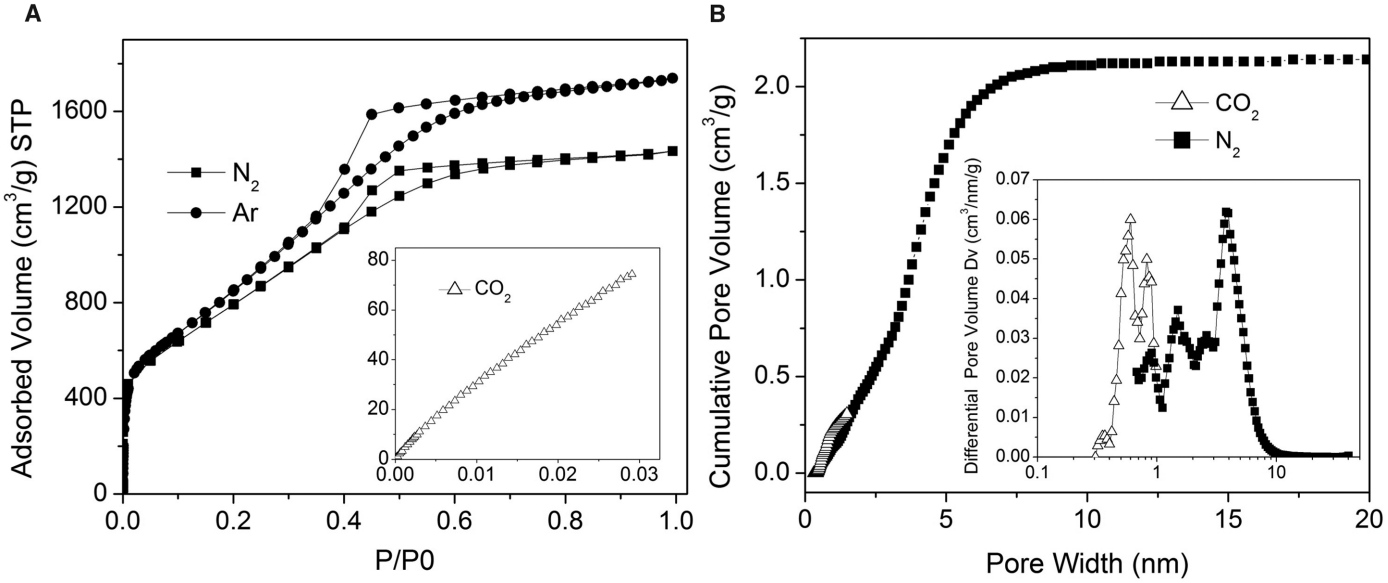

Fig. 3. Gas adsorption/desorption analysis of an a-MEGO sample (SSA ~ 3100 m^2/g). (**A**) High-resolution, low-pressure N_2 (77.4 K) and Ar (87.3 K) isotherms. (Inset) The CO_2 (273.2 K) isotherm. (**B**) Cumulative pore volume and (inset) pore-size distribution for N_2 (calculated by using a slit/cylindrical NLDFT model) and CO_2 (calculated by using a slit pore NLDFT model).

for large-scale AC-based supercapacitors—a practical energy density of above 20 Wh/kg for a packaged device is expected. This is four times higher than existing AC-based supercapacitors, two times higher than that reported for carbon-oxide hybrid electrochemical devices (*2*), and nearly equal to the energy density of lead acid batteries. At the same current density (5.7 A/g), the power density is also very high at ~250 kW/kg, as estimated by using the voltage drop and ESR obtained from the discharge curve. For a packaged cell, the power density of ~75 kW/kg is one order higher than the values from commercial carbon supercapacitors that have energy density values of 4 to 5 Wh/kg (*2*). This material is also very stable. After 10,000 constant current charge/discharge cycles at a current density of 2.5 A/g in neat BMIM BF_4 electrolyte (fig. S9), 97% of its capacitance was retained. We reasoned that this carbon might perform even better with smaller-diameter ions (*35*). With neat ethyl-methylimidazolium bis(trifluormethylsulfonyl)imide (EMIM TFSI) as electrolyte (fig. S10), the measured gravimetric capacitance of a-MEGO (SSA ~ 3100 m^2/g) at 3.5 V and a current density of 0.7 A/g is 200 F/g, with an ESR of 8.6 ohms. However, the curves in fig. S10 are not as ideal as those from a-MEGO in either BMIM BF_4/AN or TEA BF_4/AN electrolyte. Other carbons (such as CDCs) using the EMIM TSFI electrolyte have been reported with comparable performance values, although the measurements were performed at an elevated temperature (60°C) (*36*).

The high powder conductivity of ~500 S/m, a C/O atomic ratio of up to ~35, the very low H content, and the essential absence of dangling bonds in the a-MEGO suggest that it has a high content of sp^2-bonded carbon and very few edge atoms for the samples with SSA of above 2500 m^2/g. This along with the SEM, TEM, STEM, EELS, EPR, XPS, XRD, and adsorption isotherm data thus support a highly porous carbon comprised almost entirely of single sheets of sp^2-bonded carbon. This suggests that a large fraction of "negative curvature carbon" (*37*–*39*) could be present.

The excellent performance obtained for various electrolytes opens the possibility to engineer supercapacitor electrodes based on this form of carbon in order to target a wide range of applications, such as high energy, high power, or low cost. Unlike other carbon materials, no special substrates or transfer procedures are required for synthesis. For supercapacitor manufacturing, this material can be treated the same as current commercial ACs. Electrodes used for testing were of the same thickness used in commercial cells, and testing was performed using commercial collectors, separators, binders, and electrolytes. As previously stated, the processes used to synthesize this carbon electrode material are readily scalable to industrial levels. For example, we have demonstrated that this simple activation process

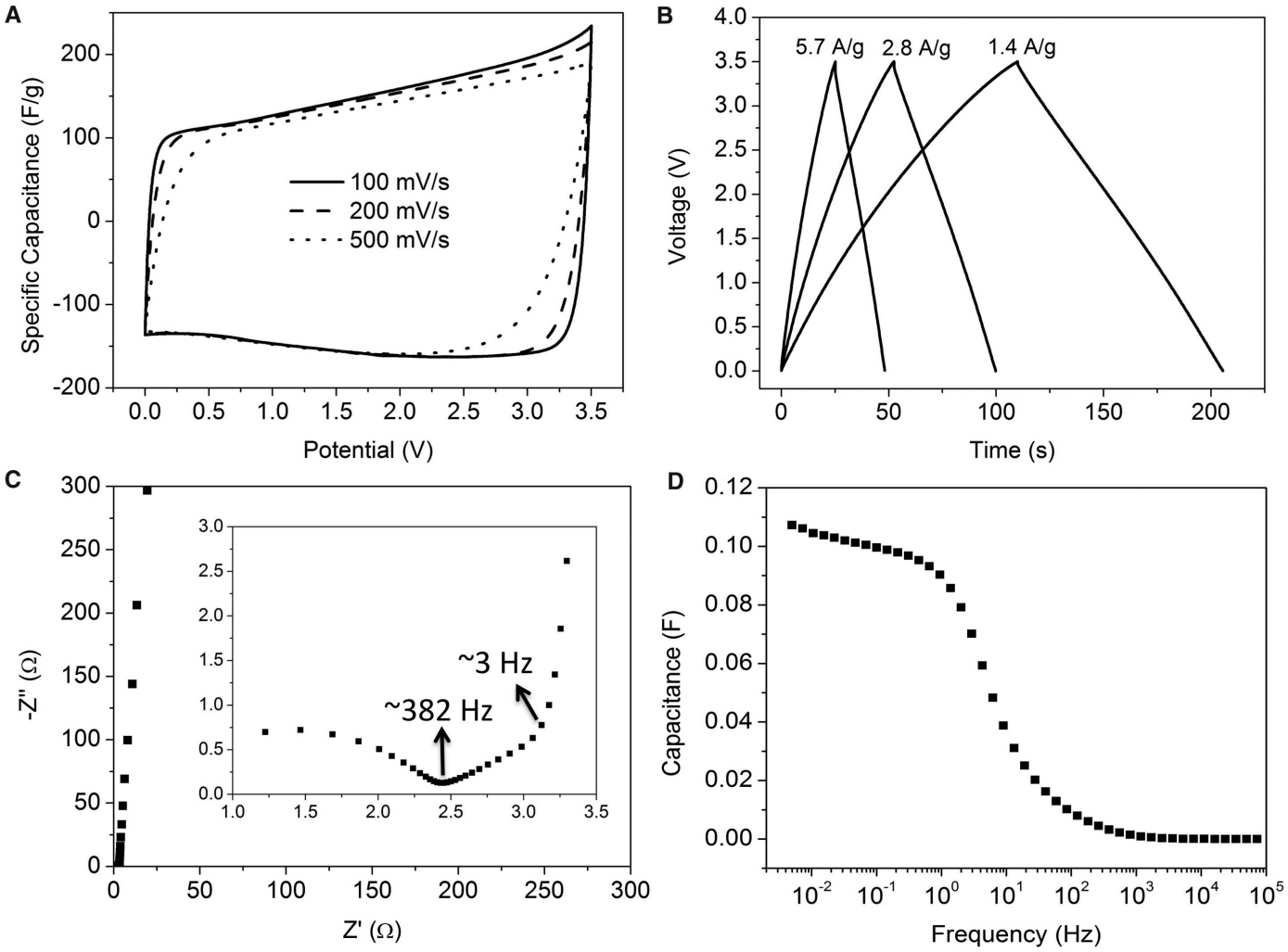

Fig. 4. Supercapacitor performance of a-MEGO (SSA ~ 2400 m^2/g) in the BMIM BF_4/AN electrolyte. (**A**) CV curves for different scan rates. Rectangular shapes indicate the capacitive behavior. (**B**) Galvanostatic charge/discharge curves of a-MEGO–based supercapacitor under different constant currents. (**C**) Nyquist plot, showing the imaginary part versus the real part of impedance. (Inset) The data at high-frequency ranges, with frequency values corresponding to the transition of the curves marked. (**D**) Frequency response of the gravimetric capacitance of the a-MEGO supercapacitor. Capacitances of 35 and ~8.8 mF remain at the frequencies of 10 and 100 Hz, respectively.

also can be applied to TEGO (figs. S11 and S12), which is already being manufactured in ton quantities (*13*). By use of this type of simple activation process already commercially demonstrated for ACs, scaled a-MEGO and a-TEGO production for advanced energy/power electrochemical electrical energy storage devices may be realized in a short period.

References and Notes

1. J. R. Miller, P. Simon, *Science* **321**, 651 (2008).
2. A. Burke, *Electrochim. Acta* **53**, 1083 (2007).
3. J. A. Fernandez *et al.*, *J. Power Sources* **175**, 675 (2008).
4. P. Simon, Y. Gogotsi, *Nat. Mater.* **7**, 845 (2008).
5. J. Chmiola *et al.*, *Science* **313**, 1760 (2006).
6. N. L. Wu, *Mater. Chem. Phys.* **75**, 6 (2002).
7. T. Brezesinski, J. Wang, S. H. Tolbert, B. Dunn, *Nat. Mater.* **9**, 146 (2010).
8. A. Rudge, J. Davey, I. Raistrick, S. Gottesfeld, J. P. Ferraris, *J. Power Sources* **47**, 89 (1994).
9. M. Toupin, T. Brousse, D. Belanger, *Chem. Mater.* **16**, 3184 (2004).
10. A. Izadi-Najafabadi *et al.*, *Adv. Mater.* **22**, E235 (2010).
11. D. N. Futaba *et al.*, *Nat. Mater.* **5**, 987 (2006).
12. Y. Zhu *et al.*, *Adv. Mater.* **22**, 3906 (2010).
13. M. Segal, *Nat. Nanotechnol.* **4**, 612 (2009).
14. M. D. Stoller, S. J. Park, Y. W. Zhu, J. H. An, R. S. Ruoff, *Nano Lett.* **8**, 3498 (2008).
15. Y. Wang *et al.*, *J. Phys. Chem. C* **113**, 13103 (2009).
16. W. Lv *et al.*, *ACS Nano* **3**, 3730 (2009).
17. Y. Zhu *et al.*, *ACS Nano* **4**, 1227 (2010).
18. S. R. C. Vivekchand, C. S. Rout, K. S. Subrahmanyam, A. Govindaraj, C. N. R. Rao, *J. Chem. Sci.* **120**, 9 (2008).
19. J. R. Miller, R. A. Outlaw, B. C. Holloway, *Science* **329**, 1637 (2010).
20. Y. Zhu *et al.*, *Carbon* **48**, 2118 (2010).
21. H. Marsh, F. Rodriguez-Reinoso, *Activated Carbon*. (Elsevier, London, 2006).
22. E. Raymundo-Pinero *et al.*, *Carbon* **43**, 786 (2005).
23. V. Barranco *et al.*, *J. Phys. Chem. C* **114**, 10302 (2010).
24. T. Liu, T. V. Sreekumar, S. Kumar, R. H. Hauge, R. E. Smalley, *Carbon* **41**, 2440 (2003).
25. M. A. Lillo-Rodenas, D. Cazorla-Amoros, A. Linares-Solano, *Carbon* **41**, 267 (2003).
26. J. A. Leiro, M. H. Heinonen, T. Laiho, I. G. Batirev, *J. Electron Spectrosc. Relat. Phenom.* **128**, 205 (2003).
27. S. D. Berger, D. R. McKenzie, P. J. Martin, *Philos. Mag. Lett.* **57**, 285 (1988).
28. P. I. Ravikovitch, A. Vishnyakov, R. Russo, A. V. Neimark, *Langmuir* **16**, 2311 (2000).
29. K. S. W. Sing *et al.*, *Pure Appl. Chem.* **57**, 603 (1985).
30. J. C. Groen, L. A. A. Peffer, J. Perez-Ramirez, *Microporous Mesoporous Mater.* **60**, 1 (2003).
31. A. V. Neimark, Y. Lin, P. I. Ravikovitch, M. Thommes, *Carbon* **47**, 1617 (2009).
32. M. D. Stoller, R. S. Ruoff, *Energy Environ. Sci.* **3**, 1294 (2010).
33. P. L. Taberna, P. Simon, J. F. Fauvarque, *J. Electrochem. Soc.* **150**, A292 (2003).
34. C. Portet, M. A. Lillo-Ródenas, A. Linares-Solano, Y. Gogotsi, *Phys. Chem. Chem. Phys.* **11**, 4943 (2009).
35. C. O. Ania, J. Pernak, F. Stefaniak, E. Raymundo-Pinero, F. Beguin, *Carbon* **44**, 3126 (2006).
36. C. Largeot *et al.*, *J. Am. Chem. Soc.* **130**, 2730 (2008).
37. S. J. Townsend, T. J. Lenosky, D. A. Muller, C. S. Nichols, V. Elser V, *Phys. Rev. Lett.* **69**, 921 (1992).
38. H. Terrones, A. L. Mackay, *Prog. Cryst. Growth Charact. Mater.* **34**, 25 (1997).
39. E. Barborini *et al.*, *Appl. Phys. Lett.* **81**, 3359 (2002).

Acknowledgments: We appreciate funding support from NSF under award DMR-0907324, the U.S. Department of Energy (DOE) under award DE-SC001951, and the Institute for Advanced Technology. The research by E.A. and D.S. has been carried out at the Center for Functional Nanomaterials, Brookhaven National Laboratory, which is supported by the DOE, Office of Basic Energy Sciences, under contract DE-AC02-98CH10886. We thank P. Stephens for XRD data collection, which is supported by DOE under contract DE-AC02-98CH10886, and P. Ercius for data collection on the TEAM instrument, supported by DOE contract DE-AC02-05CH11231. We thank M. Nilges for help with EPR. We thank J. Potts for providing graphite oxide samples. We appreciate use of equipment in K. Johnston's lab. R.M.W. and A.P. acknowledge the partial support of the GRC-NRI SWAN Center for the XPS data collection and analysis. R.S.R., Y.Z., M.D.S., and S.M. have filed a U.S. patent application (application no. PCT/US2011/036164) regarding work in this paper.

Supporting Online Material

www.sciencemag.org/cgi/content/full/science.1200770/DC1
SOM Text
Figs. S1 to S12
References
Movie S1

22 November 2010; accepted 2 May 2011
Published online 12 May 2011;
10.1126/science.1200770

Disorder-Enhanced Transport in Photonic Quasicrystals

Liad Levi,* Mikael Rechtsman,* Barak Freedman, Tal Schwartz, Ofer Manela, Mordechai Segev†

Quasicrystals are aperiodic structures with rotational symmetries forbidden to conventional periodic crystals; examples of quasicrystals can be found in aluminum alloys, polymers, and even ancient Islamic art. Here, we present direct experimental observation of disorder-enhanced wave transport in quasicrystals, which contrasts directly with the characteristic suppression of transport by disorder. Our experiments are carried out in photonic quasicrystals, where we find that increasing disorder leads to enhanced expansion of the beam propagating through the medium. By further increasing the disorder, we observe that the beam progresses through a regime of diffusive-like transport until it finally transitions to Anderson localization and the suppression of transport. We study this fundamental phenomenon and elucidate its origins by relating it to the basic properties of quasicrystalline media in the presence of disorder.

Anderson localization (*1*), a fundamental concept in solid-state physics, describes how introducing disorder can transform a conducting crystal into an insulator. This prediction and subsequent experiments have shown that, generally, disorder works to arrest transport in periodic systems containing disorder (*2*–*5*), as well as in fully random potentials (*6*–*10*). However, some systems still pose fundamental challenges to this concept—most notably, quasicrystals. Quasicrystals (QCs) (*11*, *12*) constitute an intermediate phase between fully periodic and fully disordered media: They do not have a unit cell and do not exhibit translation symmetry; nevertheless, they possess noncrystallographic rotational symmetry and long-range order and display Bragg diffraction. Although many of the properties of QCs are now well understood, some fundamental questions remain. Perhaps one of the most intriguing questions related to QCs has to do with transport. Opposite to crystals containing disorder, which exhibit Anderson localization, it has been suggested that disorder can enhance transport in QCs (*13*, *14*). Indirect experiments have indicated that in some regimes, increasing disorder could enhance transport (*14*).

Department of Physics and Solid State Institute, Technion, Haifa 32000, Israel.

*These authors contributed equally to this work.
†To whom correspondence should be addressed. E-mail: msegev@tx.technion.ac.il

The electronic structure of atomic QCs has been shown to have multifractal eigenstates (*15*, *16*), which may or may not be normalizable (thus, localized), depending on the critical exponent associated with the given state. The transport properties of QCs are directly related to the critical nature of their eigenstates, in particular, in the presence of disorder (*17*). QCs have been shown to exhibit counterintuitive transport properties, including extremely low conductivity that increases with both temperature (inverse Matheisen rule) and spatial disorder arising from structural defects (*14*). Both of these effects have been attributed (*16*, *18*) to hopping between critical states of different spatial extents near the Fermi energy (due to inelastic electron-phonon scattering for the former and elastic scattering from structural defects for the latter). This increase in transport with disorder is directly opposite to the characteristic behavior of crystals, wherein transport is reduced with increasing disorder.

Thus far, experiments on transport in atomic QCs were carried out by the study of macroscopic conductivity. However, conductivity experiments are problematic for addressing some basic questions on QCs. First, the mechanisms proposed to explain the unusual transport in QCs assume noninteracting electrons; however, conductivity measurements inevitably incorporate electron-electron interactions. Second, conductivity measurements do not allow direct observation of wave packets, which could be a key property in unraveling the mechanisms underlying transport. With the recent progress in photonic lattices (*19*), manifesting analogies between light propagating in a waveguide

Carbon-Based Supercapacitors Produced by Activation of Graphene

Yanwu Zhu, Shanthi Murali, Meryl D. Stoller, K. J. Ganesh, Weiwei Cai, Paulo J. Ferreira, Adam Pirkle, Robert M. Wallace, Katie A. Cychosz, Matthias Thommes, Dong Su, Eric A. Stach and Rodney S. Ruoff

Science **332** (6037), 1537-1541.
DOI: 10.1126/science.1200770originally published online May 12, 2011